Insights in erosion instabilities in nonconsolidated porous media

P. Cerasi[1] and P. Mills[2,*]

[1]*Laboratoire de Biorhéologie et d'Hydrodynamique Physico-Chimique, Centre National de la Recherche Scientifique*
URA No. 343, Université Paris 7–Denis Diderot, 2 Place Jussieu, 75251 Paris Cedex 05, France
[2]*Laboratoire de Physique des Matériaux Divisés, Université de Marne la Vallée, 2 rue de la Butte Verte,*
93166 Noisy le Grand Cedex, France

We investigate the different flow regimes in nonconsolidated porous media. The porous bulk is soaked with water, which is then pumped out of it, across the boundary defined by the particles at the edge of the bulk. Experiments are carried out on sand and glass beads soaked in distilled water and placed in a circular Hele-Shaw cell, the flow being radially convergent. We show, for a given value of flow velocity (the yield velocity), the existence of an unstable regime where the fluid-porous interface is deformed and branches upstream in the bulk. When this velocity is further increased, two cases arise depending on the value of the yield velocity: Either a second threshold is passed, global fluidization of the porous bulk sets in, and the flow becomes stable or the instability persists and the canal arborescence continues to grow. The driving mechanism of this instability is thus the permeability contrast across the edge of the porous bulk; when this contrast diminishes, the flow becomes stable. A force balance on the boundary particles predicts the threshold value for the fluid velocity, beyond which the flow is unstable. Using a Saffman-Taylor inspired linear perturbation analysis [Proc. R. Soc. London, Ser. A **245**, 312 (1958)], a dispersion function is found (predicting the wavelength dependence of the instability growth amplitude), taking into account the particle arch formation in the porous bulk. We then find the velocity of propagation of the receding front, predicted to be proportional to the particle velocity beyond the front, itself described by a Bagnold concentrated suspension flow [Proc. R. Soc. London, Ser. A **225**, 49 (1954)]. This front velocity is successfully confronted with experimental measurements. A screening effect characteristic of Laplacian growth phenomena is seen in the experiments as testified by flow rate conservation between the different branches of the arborescence and direct dye visualization. The topologies obtained are fractal and the measured dimension $D_f = 1.6 - 1.7$ compares favorably to the calculated dimension from the branching angle distribution. [S1063-651X(98)10610-4]

PACS number(s): 47.55.Mh, 47.20.Ft, 61.43.Hv, 64.60.Lx

I. INTRODUCTION

The problems of flow of granular materials, fracture, and erosion of nonconsolidated porous media have gained much insight recently. The solid stress distribution in a compact granular packing has been investigated both theoretically and experimentally [1–3] and a considerable amount of work has been done on avalanche phenomena and stability under flow [4,5]. A large body of work has also been published on the problems of sand infiltration in oil or water wells, leading to different analytical models [6–8]. Growing cracks have been described using lattice models in which elastic bonds are broken with different probability laws or lattice geometries [9,10]. Erosion models also rely on lattice simulations in which the soil level is calculated at each point taking into account water flow from neighboring lattice points [11–13]. In this article we look at the different flow regimes possible in a nonconsolidated porous medium [14,15], showing the existence of an erosion instability, and we propose a theoretical treatment based on a solid and fluid force balance and a Saffman-Taylor inspired stability analysis [16,17]. The porous medium is soaked with a Newtonian fluid that flows across an interface defined by the boundary of the porous bulk, in a direction from the bulk outward. We used a circu-

lar Hele-Shaw cell filled with sand or glass beads in which the soaking fluid is pumped through a hole in the center of the lower plate [18], thus establishing a radially convergent flow. A controlled normal force is applied on the upper plate in all our experiments.

Our theoretical approach differs from the models based on classical elastoplastic rupture [6–8] by taking into account the granular nature of the material through the redistribution of the normal stresses and by predicting a selective erosion regime, which we call the unstable regime. This predicted (and observed) regime stands in sharp contrast to the two stable regimes of global fluidization or liquefaction and stationary seeping flow, occurring for slightly different flow conditions. These stable regimes (in the sense of perturbation analysis) are the only ones predicted by the existing plastic yield models [6–8].

As the flow rate increases in the cell, we observe a first transition from a stable seeping regime to an unstable erosion regime. As this threshold is reached, a decompaction occurs in the porous bulk, with fractures forming near the edge [2]. In our experiments, stress arches across particle contacts form in the bulk, redirecting the forces away from the radial direction. These forces are solid-solid interactions between the bulk particles, resulting from a combination of fluid pressure and the weight of the particles. The existence of a stress threshold above which the particles begin to move is due to solid friction between the particles and the confining plates

---

*Author to whom correspondence should be addressed.

on the one hand and between the particles themselves on the other [19]. The chains of strong contact forces passing through these arches are unstable unless other particles participating in weaker force chains fill the space immediately behind the arches [20]. Thus the particles on the edge of our porous medium form unstable arches, which will be the first to collapse when the threshold is reached. The irregular interface left by the decompaction process induces local deviations from a purely radial flow, breaking the symmetry in our system (average stress distribution, isobar configuration, etc.). As the current lines converge on the tips of small breaches in the interface created by the fracturing process, these tend to grow due to the increased value of the local fluid stress, compared to other areas, which are then effectively screened. Thus particle-free waterways will develop and branch upstream in the porous bulk, *against* the direction of flow. As opposed to the now classical fluid digitation experiments, the flow in this instability is directed from a region of low permeability to a region of high permeability, whereas the interface between the two regions recedes into the zone of low permeability. Here the interface is not a meniscus between two nonmiscible fluids but simply the borderline between immobile particles and particles moving with the fluid in a suspension. Nevertheless, we show that this instability still belongs to the class of Laplacian growths, seemingly in contradiction with the predictions of the Saffman-Taylor theory, the driving mechanism being the permeability contrast across the interface. Depending on the value of the yield velocity (which varies, for example, with the external force applied on the solid porous matrix), we can predict two different evolutions as the fluid velocity is increased. A second threshold may be passed, above which the stress is everywhere strong enough to override the friction forces and the whole bulk moves, establishing a global fluidization. In fact, as the mean velocity increases near the boundary of a growing tip, a larger quantity of sediment is poured into the adjacent channel, tending to block it and thus to diminish the size of the channel and at the same time to remove the Laplacian screening, leading to a uniform movement of the front. Another case, for higher yield velocity, is the persistence of the unstable flow regime for all fluid velocities above threshold with no transition to fluidization. In this situation, the sediment poured into the growing canals is evacuated faster than the receding tip of the waterways. Thus the canals are characterized by a very high permeability (as compared to the porous bulk) resulting in the persistence of the Laplacian screening and hence of the unstable state.

It may be helpful to consider, at first, a different problem showing an analogy to our experiments, namely, the silo problem. A narrow container is filled with a granular material, sand, for example, and the weight of the particles is recorded as a function of the heap's height [2,21]. It is found that part of the stress is redirected at the wall of the cylinder, making the weight plateau at a constant value, independently of any further increase in height. The formation of particle arches in the granular medium is responsible for this stress redistribution, with the uppermost particles pressing sidewise on the lower ones. Furthermore, if the lower confining boundary is suddenly removed, a distribution of fractures appears in the column during the decompaction process [2]; this distribution presents a power-law dependence on the size
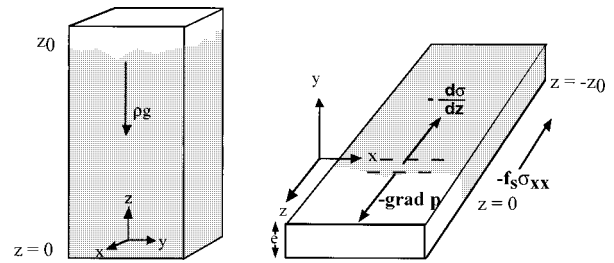

FIG. 1. Analogy with the silo problem in planar geometry. On the left is a column of sand fractures under its own weight when the lower boundary is removed and on the right are cracks form near the interface of sand particles under water flow.

of the cracks, indicating that all sizes are represented (scale-independent distribution). A similar phenomenon is observed in our experiments with sand, at the flow-induced stress threshold; cracks appear in the porous bulk while it is loosening up, exhibiting as well a power-law dependence on size. The alteration of the flow characteristics near such cracks is responsible for the onset of the instability, which we will now analyze in more detail.

II. THEORY

We establish a theoretical model of the erosion instability by first examining the stress distribution in a compact granular heap and its stability under external forces such as gravity or the fluid pressure gradient in our experiences. This analysis gives us the expression of two yield velocities corresponding to a decompaction of the bulk and a transition to the erosion instability. The instability is due to the permeability contrast across the interface; when this contrast is weakened, the instability is killed and global fluidization sets in. Since the instability is believed to belong to the Laplacian growths class, the permeability contrast can be erased only if the Laplacian screening can be avoided and the growing waterways filled with bulk particles. In the framework of a linear stability analysis, by supposing the existence of a small sinusoidal perturbation of the interface, writing the continuity of pressure and flow rate as well as mass conservation across the interface, and adding the expression of the unstable yield velocity, we arrive at a dispersion equation (relating the instability growth coefficient s to the canal width wave number k). This equation is then reconsidered to take into account the effects of the formation of particle arching in the porous bulk. We then express the particle velocity and the decompaction wave velocity in the different regimes, depending on the value of the yield velocity; we thus find the conditions for global fluidization to take place. The nonlinear regime is also briefly described and the fractal dimension of the arborescences predicted.

A. Solid stress distribution due to Darcian flow in a granular heap

To simplify matters, we will consider a planar geometry and use the silo analogy (see Fig. 1). Indeed, in the same way that the dry granular heap in the silo is subject to the action of the constant force of gravity, the bulk in our cell is subject to the pressure gradient force (which is constant in planar geometry) and the same redistribution of stress occurs in

both experiments, due to solid static friction. In terms of volume forces, the analogy is then

$$\rho \vec{g} \leftrightarrow \text{grad } p. \qquad (1)$$

The normal stress distribution is described by the Janssen hypothesis [22]

$$\sigma_{xx} = K\sigma_{zz}, \qquad (2)$$

with the sharing coefficient $0 < K < 1$, and the Coulomb friction force is written as

$$\sigma_{zx} = f_s \sigma_{xx}, \qquad (3)$$

where f_s is a static solid friction coefficient. We next write the force balance at equilibrium for unit bulk volume by considering the force that should be applied at the interface to maintain the bulk in place [1]:

$$\frac{\partial \sigma_{ij}}{\partial x_j} + \frac{dF_{exti}}{dV} = 0, \qquad (4)$$

$$-\frac{d\sigma}{dz} - \frac{2f_s}{e} K\sigma + |\text{grad } p|_z = 0 \qquad (5)$$

for our experiment, with $\sigma_{zz} = \sigma$ and e the width of our Hele-Shaw cell (or a unit width in the silo bulk). $-d\sigma/dz$ is the volume force needed to counteract the fluid force pushing on the bulk. This normal stress variation is a direct consequence of the Janssen relation. The solution of Eq. (5) is

$$\sigma = \lambda |\text{grad } p| \left[1 - \exp \frac{-(z + z_0)}{\lambda} \right], \quad z_0 > 0, \qquad (6)$$

where $\lambda = e/2Kf_s$ is the Janssen screening length. We assume the external applied force to be much larger than the internal vertical pressure distribution due to gravity in the porous bulk, allowing us to neglect a ρg term in Eq. (5). The first derivative of Eq. (6) evaluated at the interface gives us the external force needed to maintain equilibrium in the bulk:

$$\frac{d\sigma}{dz} = -|\vec{\nabla}p| e^{-(z+z_0)/\lambda},$$

$$-\frac{d\sigma}{dz}\bigg|_{z=0} = \frac{2f_s P}{e} \Rightarrow |\vec{\nabla}p| = \frac{2f_s P}{e}.$$

In the latter equation P is the external pressure associated with the confining force exerted on the bulk. As the bulk may fracture, we took the maximum value of the force ensuring equilibrium, that is, $z_0 \to 0$. The stability condition for the bulk as a whole is thus given by

$$|\text{grad } p|_{\text{yield}} = \frac{2f_s P}{e},$$

which, combined with Darcy's law $\vec{v} = (-a^2/\alpha\mu)\text{grad } p$, gives an estimate of the velocity needed for decompaction:

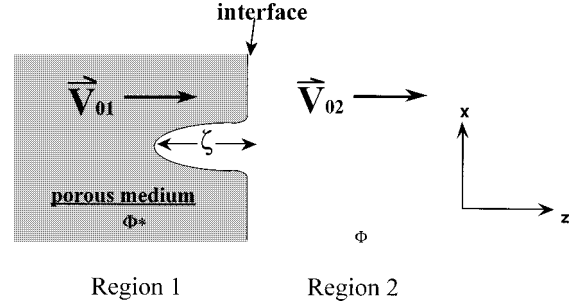$$\bar{v}_{\text{dec}} = \frac{2a^2}{\alpha\mu} \frac{f_s P}{e}, \qquad (7)$$

FIG. 2. Porous medium's boundary in a planar Hele-Shaw cell as seen from above. The packing volume fraction is represented by Φ^* and the particle suspension resulting from porous bulk loosening and separation is denoted as Φ. A small perturbation of the interface is shown and the arrows indicate the direction of the mean nonperturbed fluid velocities.

where a is the average size of the particles, μ the fluid viscosity, and α^{-1} the porous permeability. In the same way, one can estimate the first yield velocity (corresponding to the instability threshold) by writing the same balance of forces on one particle:

$$|\text{grad}(p)|_{\text{yield}} a^3 = 2f_s P a^2$$

leading to

$$\bar{v}_y = 2\frac{a}{\alpha\mu} f_s P. \qquad (8)$$

An important point remains to be clarified: Why should only the first rows of porous particles be detached from the bulk at the threshold? To answer this question we will suppose that a crack appears at a distance z' from the interface (defined by $z = 0$) so as to separate the particles into two distinct blocks, which we will call block 1 and block 2.

Just as the blocks are about to move, we can write the force equilibrium equation (5) for each block:

$$-\frac{d\sigma_1}{dz} = |\text{grad } p| e^{(z'-z_0)/\lambda}, \quad z_0, z' > 0$$

$$\qquad \qquad \qquad \qquad \qquad \qquad \qquad (9)$$

$$-\frac{d\sigma_2}{dz} = |\text{grad } p| e^{-z'/\lambda}.$$

This is the force per unit volume that must be applied in order to maintain each block in position. As $z' \to 0$, the force needed to maintain block 2 in place approaches its maximum value $|\text{grad } p|$. Thus the cracks near the bulk edge will grow first since the force that would be needed to maintain them in place is always higher than that needed for the other blocks and the edge particles will therefore be the first to leave the bulk.

B. Linear stability analysis of the interface

We will now write the stability condition for the porous interface, using a classical perturbation approach [16]. Figure 2 shows the interface, in planar geometry. The fluid pressure field in the porous medium (region 1) and outside it (region 2) in a Hele-Shaw cell satisfies, if incompressible,

$$\nabla^2 p = 0. \tag{10}$$

The velocity field will be denoted by

$$v_1 = v_{01} + \delta v_1, \quad v_2 = v_{02} + \delta v_2, \tag{11}$$

where v_{01} and v_{02} are the nonperturbed fluid velocities in the porous bulk and outside it, respectively, with the perturbations δv_1 and δv_2. To zeroth order, the pressure field can be written, using Darcy's law in region 1 and a similar law for a two-dimensional (2D) viscous flow in region 2,

$$p_0 = \begin{cases} -\alpha_1 v_{01} z, & z < 0 \\ -\alpha_2 v_{02} z, & z > 0. \end{cases} \tag{12}$$

We now introduce a small sinusoidal perturbation of the interface between the porous particles and the fluid (at the boundary between regions 1 and 2) of amplitude $\zeta \sim \exp[ikx + st]$. At first order, we take a similar pressure perturbation field

$$\delta p_1 \sim \varphi_1(z) \exp[ikx + st],$$

$$\delta p_2 \sim \varphi_2(z) \exp[ikx + st]$$

and by Eq. (10) we find (retaining the physical solution)

$$\varphi_1 = \varphi_{01} e^{kz}, \quad \varphi_2 = \varphi_{02} e^{-kz}. \tag{13}$$

This perturbation induces a corresponding perturbation in the velocity field, given by Eq. (12) (for small z):

$$\alpha_1 \delta v_1 = -\frac{\partial(\delta p_1)}{\partial z} \approx -k\varphi_{01}\zeta,$$

$$\alpha_2 \delta v_2 = +k\varphi_{02}\zeta. \tag{14}$$

1. Dispersion equation

The velocity u of the interface can correspondingly be written as

$$u = u_0 + \delta u = -\frac{dz}{dt} \tag{15}$$

and the perturbation velocity

$$\delta u = -\frac{d\zeta}{dt} = -s\zeta.$$

u is the velocity with which the decompaction wave recedes through the porous bulk. We now write the dispersion equation associated with the instability's growth:

$$s\zeta = -G\delta v_1, \tag{16}$$

where G is a function of the fluid velocity v_1 and the yield velocity v_y. In order to find the explicit form of this function, we will first look at the flow of particles immediately behind the front. Conservation of mass across the receding interface (as written for the solid particles) gives
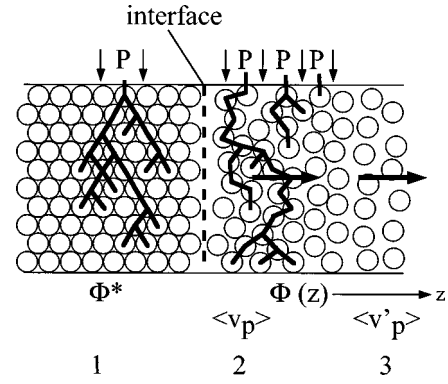
$$-u(\Phi^* - \Phi) = \Phi v_p, \tag{17}$$

FIG. 3. Schematic illustration of the interface as the porous bulk is undergoing decompaction. In region 1, before the front, the particles are immobile and the packing is maximal ($\Phi = \Phi^*$). In region 2, just after the front, the bulk is dilating and the particles begin to move with the Bagnold velocity v_p. In this region, the particles experience the external applied pressure P and an additional pressure ΔP due to the dilatation. The volume fraction is slightly lower than that in region 1 (again, because of the dilatation). In region 3, the particles begin to be carried away by the fluid and no longer "feel" the outside pressure P. The volume fraction diminishes with the distance from the front.

where Φ^* is the bulk volume fraction and Φ the volume fraction after decompaction, just beyond the front; v_p is the particle velocity at the onset of decompaction. A slight dilatation is associated with this decompaction, leading to a difference of volume fraction across the front not bigger than 10%. Thus (for $\Phi \sim \Phi^*$)

$$-u = \frac{\Phi^* v_p}{\Delta\Phi} = \kappa_1 v_p \quad \text{with} \quad \kappa_1 > 1. \tag{18}$$

Beyond the front, the particles of the dilating bulk experience a pressure $P + \Delta P$ due to the external force applied on the cell combined with the increase in interparticle force associated with the dilatation [23] (region 2 in Fig. 3).

The mean particle velocity in this configuration can be calculated with the Bagnold equation [23]

$$-\gamma \frac{d}{dy}\left(\frac{dv_p}{dy}\right)^2 - \frac{\partial p}{\partial z} - \frac{2f_s P}{a} = 0, \tag{19}$$

or

$$-\frac{d}{dy}\left(\frac{dv_p}{dy}\right)^2 + \frac{V^*}{a^3}(v_1 - v_y) = 0,$$

the solution of which is

$$\langle v_p \rangle = \int_0^{e/2} v_p \, dy \Big/ \int_0^{e/2} dy = CV^{*1/2}(v_1 - v_y)^{1/2}, \tag{20}$$

with

$$C = \frac{\sqrt{2}}{10}\left(\frac{e}{a}\right)^{3/2}, \quad V^* = \frac{\alpha\mu}{\gamma},$$

where again e is the cell gap, a the particle size, α^{-1} the permeability, μ the fluid's viscosity, and γ a constant relat-

ing the momentum transfer between particle layers to the dilatation pressure, which depends on the particle characteristics [23]. From here onward, the angular brackets in the notation of the average particle velocities will be dropped without ambiguity since we will not deal with the instantaneous velocities. At this point, we wish to stress that the Bagnold flow formalism adopted here may not be the best choice, as it concerns collision driven granular flow and not solid friction dominated granular flow, as in our case. Recent experiments as well as computer simulations [24] would seem to point to an exponent 1 instead of 1/2 in Eq. (20), even though the flow geometry is quite different in our experiments (confined flow vs open channel flow; see the discussion in [24]). However, there are no well defined behavior laws for concentrated suspensions exhibiting dry friction as for now and as we will see in Sec. III, Bagnold's law is apparently well verified in our case, at least near the threshold.

We can now introduce the Bagnold velocity in relation (18) and develop the fluid velocity to first order:

$$u = -\kappa_1 CV^{*1/2}(v_{01} - v_y + \delta v_1)^{1/2}.$$

At the threshold, this equation is nonlinear and we cannot pursue our analysis:

$$v_{01} = v_y, \quad u = -\kappa_1 CV^{*1/2}(\delta v_1)^{1/2}. \quad (21)$$

For higher velocities, this expression can be linearized

$$v_{01} > v_y, \quad u = -\kappa_1 CV^{*1/2}(v_{01} - v_y)^{1/2}\left[1 + \frac{\delta v_1}{2(v_{01} - v_y)}\right]. \quad (22)$$

By solving Eq. (14) for the pressure perturbation and considering pressure continuity across the interface (see the Appendix) we arrive at the dispersion equation

$$s = \frac{\kappa_1 CV^{*1/2}}{2}\frac{v_{01}}{(v_{01} - v_y)^{1/2}}\left[\frac{\alpha_1 - \kappa'\alpha_2}{\alpha_1 + \kappa'\alpha_2}\right]k, \quad (23)$$

where s is the amplification factor, k' the wave number associated with the interface perturbation, and κ' a constant given in the Appendix. The α_i are given by the Kozeny-Carman [25] relation and a similar relation for 2D viscous flow on the other side of the interface:

$$\alpha_1 = \alpha_{10}\frac{\mu_0}{a^2} \quad \text{with} \quad \alpha_{10} = 180\frac{\Phi^{*2}}{(1 - \Phi^*)^2},$$

$$\alpha_2 = \alpha_{20}\frac{\mu(\Phi)}{e^2}, \quad \alpha_{20} = 12. \quad (24)$$

Equation (23) implies a linear $s(k)$ relationship, in agreement with our Laplacian growth supposition, that is, amplification of large wave numbers preferentially. However, we must now take into account the stabilizing effect of particle arches present in the bulk. Let us write the force balance on such an arch of characteristic size ξ:

$$\text{grad } p\,\xi^3 = 2f_s P a^2,$$

giving us a new estimate on the threshold velocity:

$$\tilde{v}_y = 2f_s P\frac{a}{\alpha_{10}\mu_0}(ka)^3.$$

When $ka = 1$ we recover the former yield velocity $\tilde{v}_y = v_y$. This leads us to a new dispersion equation

$$s = \frac{\kappa_1 CV^{*1/2}}{2}\frac{v_{01}}{[v_{01} - v_y(ak)^3]^{1/2}}\left[\frac{\alpha_1 - \kappa'\alpha_2}{\alpha_1 + \kappa'\alpha_2}\right]k. \quad (25)$$

A cutoff wave number [which is different from the physical cutoff associated with the particle size in Eq. (23)] appears, shifting the smallest canal widths that will develop in the unstable regime to larger length scales:

$$k_{\text{cutoff}} = \left(\frac{v_{01}\alpha_{10}\mu_0}{2f_s P a^4}\right)^{1/3}. \quad (26)$$

For 200-μm particles with a water flow rate equal to 2 ml/mn and an external confining pressure of 300 Pa, which is equivalent to 1 kg on an upper cell plate of 10 cm diameter, the shift in wave number is from $k_{\text{cutoff}}a = 1$ to 0.17 in Eq. (26), corresponding to a shift from $\lambda_c = 200\ \mu$m to a minimal branch width of $\lambda_c = 3.6$ mm.

2. Instability phase diagram

A small distance downstream, the particles flow in a concentrated suspension [with $\Phi(z)$ decreasing with z, the distance from the interface, as in region 3 in Fig. 3]. Two cases arise, depending on the ratio of the particle flux $\Phi v_p'$ downstream of the front and the decompaction flux $\Phi^* v_p$. (a) If $v_p' > \kappa_1 v_p$ then the particles downstream of the front are evacuated more rapidly than the incoming flux of freshly decompacted bulk particles, with a very small apparent volume fraction, i.e., $\Phi \to 0$. (b) On the contrary, if $v_p' < \kappa_1 v_p$ then the decompaction front recedes into the bulk faster than the rate of evacuation of the particles downstream, with the effect of plugging the newly created channel ($\Phi \sim \Phi^*$). In this situation of concentrated suspension flow, Bagnold's equation still applies and we can write the downstream average particle velocity as (no friction term)

$$v_p' = CV^{*1/2}v_1^{1/2}. \quad (27)$$

This last flow regime is thus stable and corresponds to global fluidization, the transition occurring for low values of the threshold velocity. The value of the second threshold velocity is given by (Fig. 4)

$$\kappa_1 CV^{*1/2}(v_1 - v_y)^{1/2} = CV^{*1/2}v_1^{1/2},$$

$$v_y' = \frac{\kappa_1^2}{\kappa_1^2 - 1}v_y. \quad (28)$$

Above this second threshold, the permeability contrast is very low (the Laplacian screening is lost). The unstable regime, for low v_y, is thus restricted to the interval $[v_y, v_y']$.

For higher yields, i.e., if the decompaction occurs at higher fluid velocities, the particles will be washed away with a velocity v_p' comparable to the fluid velocity v_2 very close behind the front. Thus, as Φ will be negligible compared to Φ^*, we can write [case (a)]
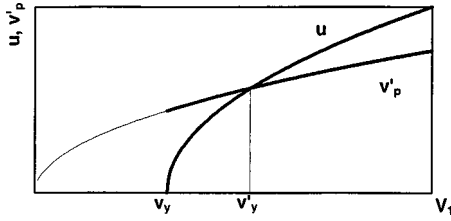
FIG. 4. Velocity u of the receding front and Bagnold downstream particle velocity v'_p in the case of low threshold velocity. The unstable regime is restricted to the interval between v_y and v'_y as the newly formed channels cannot be evacuated by the fluid rapidly enough to ensure Laplacian screening beyond v'_y (the channels collapse and the porous bulk is entirely fluidized).

$$v'_p \approx v_2 \approx \frac{1}{1-\Phi^*} v_1 = \kappa_2 v_1 > \kappa_1 v_p. \qquad (29)$$

Here the Laplacian screening will persist.

For any value of v_1 above the threshold, v'_p will be bigger than u. In the limiting case, the v_1 value for which v'_p is equal to u marks the transition back to the Bagnold regime described above (Fig. 5):

$$\kappa_1 C V^{*1/2} (v_1 - v_y)^{1/2} = \kappa_2 v_1$$

and:

$$v_{y\ trans} = \frac{1}{4} \left(\frac{\kappa_1^*}{\kappa_2} \right)^2 = \frac{V^*}{200} \left(\frac{\kappa_1}{\kappa_2} \right)^2 \left(\frac{e}{a} \right)^3. \qquad (30)$$

We can summarize the different results obtained above by drawing a phase diagram illustrating the various flow configurations (Fig. 6).

C. Nonlinear regime

When the yield velocity v_y is above the Bagnold viscous transition value $v_{y\ trans}$ and the fluid velocity v_1 is well above v_y, we are in the unstable and nonlinear flow regime. It is in this regime that the canal arborescences develop most quickly.

The arborescence develops primarily at the tips, but in the fully developed unstable regime, lateral erosion also sets in, widening the lower-order branches. To within a numerical constant, the average flow rate in one branch (of thickness λ and height e) is given by
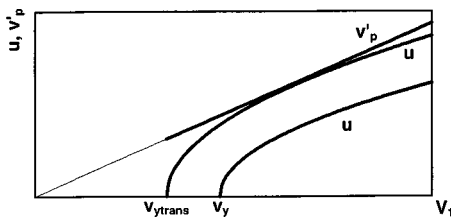

FIG. 5. Front velocity u and downstream particle velocity v'_p in the case of high threshold velocity. Here the particles are carried away with the fluid faster than the receding front, keeping the growing channels from clogging. The high channel permeability induces converging current lines on their tips, thus ensuring their growth and maintaining the Laplacian screening. The limiting case is also shown, defining the transition yield velocity $v_{y\ trans}$.
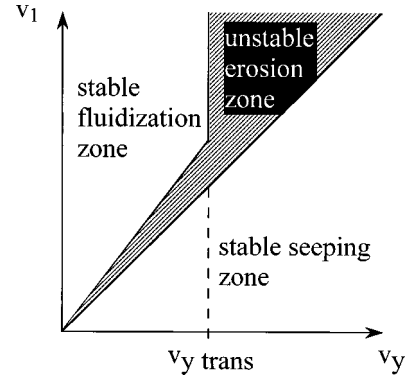

FIG. 6. Phase diagram showing the different flow regimes as a function of the first threshold velocity. The last depends on the amount of force exerted on the cell, the particle shape and size, and the gap width between the plates of the cell. On the left of the transition yield velocity $v_{y\ trans}$, the particle flow is always that of a concentrated suspension and can be described by the Bagnold equation (both in the narrow unstable region and in the fluidized state). On the right of $v_{y\ trans}$ the particles flow in a diluted suspension, which can be assimilated to a viscous flow. Because of the Laplacian screening, there is no transition back to a stable fluidization regime.

$$q_\lambda = \langle v \rangle e \lambda \approx e^2 \lambda \tau_w / \mu_0,$$

where τ_w is the wall shear stress. As the flow rate increases, so does the wall stress, until it reaches the lateral erosion yield τ_0. Above this threshold, λ increases, causing at the same time a decrease in the wall shear stress. We can thus write for the steady state

$$q_\lambda \approx e^2 \lambda \tau_0 / \mu_0.$$

Conservation of flow rate between the n order-λ branches and the parent branch gives

$$n_\lambda q_\lambda = \text{const} = q_0,$$

which implies

$$n_\lambda \lambda = \lambda_0. \qquad (31)$$

III. EXPERIMENTAL RESULTS

Our experimental setup consists of a circular Hele-Shaw cell with a 2-mm hole drilled in the center of the lower plate. A plastic tube connects this hole to a syringe mounted on a high precision pump, with which we impose the flow rate in the cell (the flow is radially *convergent* and the interface we analyze is materialized by the circular edge of the solid matrix near the central hole). We take sand or spherical glass beads for the nonconsolidated porous medium and distilled water for the fluid. The sand granulometry gives particle sizes centered on 250 μm, while the glass beads we used consist of two sizes, centered on 40 and 200 μm. The spacing between the plates varies from a minimum of about three layers of superimposed particles up to about ten layers. The permeability of the sand was measured and found to be 167 Darcy. We recorded the experiments with a video camera and stored the images on a computer equipped with an image analysis program [26]. Figure 7 shows three erosion patterns

FIG. 7. Branching topology obtained in unstable pumping of water from sand particles (with a size of ~ 250 μm and flow rate of 8 ml/mn on the left) and from spherical glass beads (with a size of ~ 200 μm and flow rate of 4 ml/mn in the middle and size of ~ 40 μm and flow rate of 0.08 ml/mn on the right).

obtained with sand and glass beads.

The topology of the figures obtained in the intermediary unstable regime depends strongly on the shape and the size of the constitutive porous particles, as well as on the force applied on the particles via the upper plate. Irregular sand particles will tend to form much more stable arches than spherical glass beads will and applying a large force on the upper plate will consolidate these arches even more. According to Eq. (8), we expect to find a linear dependence of the unstable threshold velocity with external applied force in our experiment, rather nicely confirmed in Fig. 8.

The different topologies in Fig. 7 illustrate two different paths followed in the phase diagram of Fig. 6. In the experiment with sand, the yield velocity was about 50 times higher than that needed to move the smallest glass beads and no global fluidization could be observed, independently of the fluid velocity ν_1. We are thus in the case of a vertical path to the right of $\nu_{y \text{ trans}}$, in the unstable region.

On the other hand, in the experiment with the small beads, the figure took 20 times longer to materialize as compared to the sand. The width of the unstable regime, in terms of flow rate, is very narrow, probably since the contact surface between the beads themselves and between the beads and the walls is much smaller than the contact surface in the case of sand. Thus, in our radial configuration, in which the velocity increases as $1/r$ towards the center for a given flow rate, one can have a situation where the three flow regimes coexist simultaneously; the central part is fluidized, followed immediately by an unstable zone where cracks appear, while the outer region's particles remain immobile in a steady seeping regime. In this case, the yield velocity being very low, we

are following a path to the left of $\nu_{y \text{ trans}}$; the comparatively small value of ν_1 in the narrow unstable region explains the larger amount of time needed to obtain a complete arborescence [as $s(k) \sim \sqrt{\nu_{01}}$]. Near the center of the cell, ν_1 is already above ν_y and, by Fig. 6, we are in the fluidized regime.

If we focus our attention on one given crack, we notice that the inner boundary is close to the fluidized region whereas the outer boundary is near the stable seeping zone. Thus a crack can be viewed as an expanding pocket of fluid since the inner boundary is moving faster towards the center than the outer one. Actually, a crack is never quite homogeneous in terms of width, the wider part tending to expand faster and the net result being a rotation at the same time as the crack is widening. The different cracks will then join to form the observed arborescence.

By adding glycerol in different proportions to the distilled water, we changed the viscosity of our fluid and investigated the effect on the yield flow rate, again verifying Eq. (8), i.e., finding a μ^{-1} dependence of Q_y. When plotting the yield flow rate as a function of the porous bulk thickness we find a linear $Q_y(e)$ relationship, which implies, again by Eq. (8), the existence of a constant yield velocity (in a given portion of porous bulk, at a certain distance from the center in our circular geometry; in a planar cell, this yield velocity would be constant in the whole porous matrix). However, as the thickness is further increased, the uppermost particle layer tends to be washed away before the rest of the bulk (which remains stable) and there is a departure from the linear law. This can be understood by the fact that we neglected the static pressure due to the weight of the particles themselves in the derivation of Eq. (6): When e becomes large, or the external confining pressure P on the plates is kept very low, $P \sim \rho g e$ and thus in Eq. (8) the yield velocity is now proportional to $\rho g e$ (and the flow rate quadratic in e). The upper layers will then experience a lower yield velocity, since they support fewer particles, and will be washed away first.

In our experiments it would seem that whereas the crack distribution for sand particles seems to be a power law, the distribution for spherical glass beads cannot be fitted by such a law. This might be understood in the following manner. Since the beads have a smaller contact surface relative to the sand particles and are more dispersed in size, small cracks will tend to be filled by neighboring beads, whereas in sand these cracks would stay stable due to sterical constraints (i.e., small arches are more stable in sand or nonspherical particle porous media).
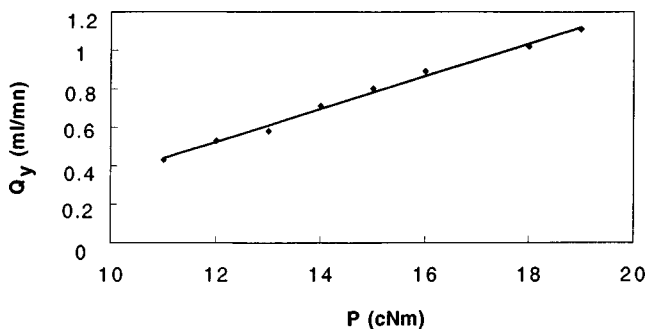

FIG. 8. Linear variation of the first threshold flow rate, and hence velocity, as a function of applied external pressure on the Hele-Shaw cell (represented here by the torque applied on a dynamometric screwdriver used to tighten the upper plate).
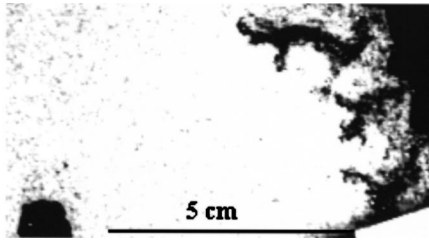
FIG. 9. Injection of water into sand in the circular cell. The central hole is visible on the lower left corner and the erosion instability is apparent on the outer boundary (with a flow rate of 30 ml/mn initially, which is then decreased by 1 ml/mn every 10 s).

We also tried to inverse the flow in our cell, that is, to inject water from the central hole into the porous bulk (radially *divergent* flow) to watch if we could obtain the same erosion instability on the outer boundary of the bulk. We did this to dismiss the suspicion that the figures obtained could be an artifact of the flow geometry since we had no success with experiments carried out in planar cells (the fluid always short-circuits the bulk via the side walls of the cells). Due to the fact that the inverse flow is divergent, the instability appears at quite higher flow rates than in convergent flow (Fig. 9).

In all our experiments we were able to determine a fractal dimension, usually lying in the range $D_f = 1.6–1.7$, generally slightly lower than the dimension corresponding to diffusion limited aggregation in two dimensions. We measured the mean branching angle for different branching orders and found an average overall value of 50.44°. One can calculate the fractal dimension of such a dichotomic arborescence knowing the average branching angle if one supposes that the arborescence grows in a Laplacian field [27]. In our case, the calculation predicts a theoretical dimension of 1.64, confirming the direct dimension measurements (obtained both by the box counting method and by the mass-radius method on binarized images).

Another feature of Laplacian growth is the screening effect due to the convergence of fluid current lines at the tips of growing branches: The entire flow is concentrated in the eroded waterways, with no seeping through the porous bulk. As we established in Sec. II [see the paragraph leading to Eq. (31)], this implies that $n_\lambda \lambda = \lambda_0$, where n_λ is the number of branches of width λ and λ_0 is the width or the parent branch (see [14]).

Image subtraction gives us a nice illustration of the symmetry breaking in the transition between the fracturing of the porous medium and the unstable regime associated with the growth of an arborescence (Fig. 10). An image is recorded just as the experiment is begun and is subtracted from another image taken somewhat later. The result is a map of the particles that moved during the time interval between the two images. Just at the flow rate threshold, one can see an isotropic distribution of fractures, their imprint remaining visible as the branches begin to grow, this time in an anisotropic manner.

Finally, we measured the front velocity u as a function of the flow rate Q. By recording a series of images during an experiment and then subtracting successive images, only the particles that have moved in the known time interval will leave a trace on the resulting image. Thus the evolution of the front can be followed and its velocity evaluated. Differ-
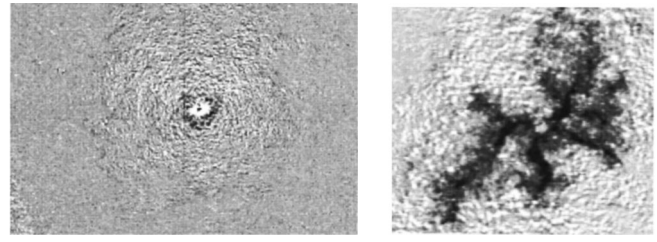

FIG. 10. Evidence of the movement of porous particles at the threshold (on the left) revealed by subtraction of successive images. At higher flow rates, erosion takes over, breaking the radial symmetry (on the right).

ent experiments were done, both with the small glass beads and with a thick layer of sand loosely tightened so as to lower the yield velocity. We were thus able to observe fluidization and record a well defined front in both cases. Figure 11 shows the experimental data fitted by Eqs. (18) and (20), implying a Bagnold flow for the particles. However, for larger flow rates and hence front velocity, a departure from Bagnold's relation is observed. The reason for this deviation is still unclear and could be attributed either to the fact that Bagnold's relation ceases to be valid for higher particle velocity or to the poor resolution of the data with this experimental method. Indeed, when the front velocity exceeds a certain value, there is a big uncertainty in the follow-up of
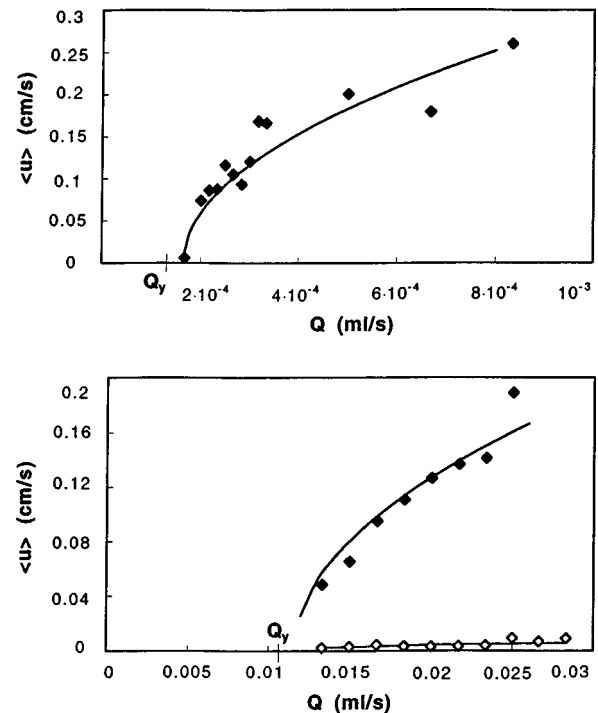

FIG. 11. Relation between the measured front velocity and the imposed flow rate. The data are fitted by Eqs. (18) and (20). The upper graph corresponds to experiments done on the small glass beads, whereas the lower graph corresponds to sand. The hollow symbols show the average particle velocity (also fitted by a Bagnold curve), which is well below that of the front in the fluidized regime. The average is taken on different experiments (for each value of flow rate) and on the different measurements (again for each value of the flow rate) for each experiment and the measured values are corrected to take into account the radial experimental geometry.

the front between two successive images (unfortunately, we could not sharpen the time resolution in the acquisition of consecutive images).

IV. CONCLUSION

We showed the existence of a hydrodynamic instability regime in a nonconsolidated porous medium, when the soaking fluid flows across the bulk out of the porous medium. The model we propose can be adapted to a wide variety of erosion phenomena, especially in stratified layers such as riverbeds. Although the theoretical treatment is very similar to that of a classical viscous fingering instability, there is an important difference in the fact that here only one fluid is present and the deformed interface of the bulk moves in the opposite direction to the fluid flow. Also, the transition between the stable and unstable regimes occurs while both the fluid and the porous grains are in movement (since we first have a decompaction and fracturing in the bulk that prepare, in a way, the perturbation of the interface, which consequently gives rise to an amplification of the curvature of parts of the boundary). Thus this instability is not stationary and is strongly nonlinear at the transition. Although the stress line configurations between the particles are fairly complicated at the onset of the instability, we showed that it nevertheless belongs to the class of Laplacian growths. Finally, we saw that the presence of arches in the bulk or, more generally, the size and shape of the constitutive particles influence strongly the topology of the figures obtained.

The particle flux has been shown experimentally to be a square root function of the control parameter of the instability, the fluid velocity. The movement of the bulk particles undergoing decompaction can therefore be accurately described by Bagnold's equation and depending on the effective permeability contrast across the interface, the flow can be stabilized or remains unstable. We thus show that different flow regimes can exist, depending on the value of the yield velocity and the outside force exerted on the cell. These flow regimes are represented in a phase diagram, on which we are able to visualize the distinct paths corresponding to our different experiments (with sand or glass beads, at different flow rates and external force).

The erosion avalanche mechanism and the volume fraction function $\Phi(z,t)$ in the unstable regime are still poorly

understood. We nevertheless are able to describe certain features of the nonlinear growth regime, such as its fractal dimension. To gain more insight into the transition into the nonlinear regime, computer simulations are now planned. Also, the influence of the third dimension (for larger gaps or 3D flow) on the erosion patterns will be investigated.

APPENDIX: DERIVATION OF THE DISPERSION EQUATION

From Eq. (22) we isolate the first-order terms

$$s\zeta = -\tfrac{1}{2}\kappa_1 CV^{*1/2}(\nu_{01}-\nu_y)^{-1/2}\delta\nu_1 .$$

We solve the system (14) for φ_i and replace $\delta\nu_1$ from the above equation:

$$\varphi_{01} = \frac{2\alpha_1(\nu_{01}-\nu_y)^{1/2}}{\kappa_1 CV^{*1/2}}\frac{s}{k},$$

$$\varphi_{02} = -\frac{2\alpha_2(\nu_{01}-\nu_y)^{1/2}\kappa'}{\kappa_1 CV^{*1/2}}\frac{s}{k}. \tag{A1}$$

In the latter equation of the system (A1), we replaced $\delta\nu_2$ by $\delta\nu_1$ through the flow conservation equation

$$(1-\Phi^*)\delta\nu_1 = (1-\Phi)\delta\nu_2 ,$$

$$\Phi^* - \Phi = \Delta\Phi \Rightarrow \delta\nu_2 = \left(\frac{1-\Phi^*}{1-\Phi^*+\Delta\Phi}\right)\delta\nu_1 = \kappa'\delta\nu_1 . \tag{A2}$$

The pressure continuity equation can be linearized at the interface, giving

$$p_1 + \delta p_1 = p_2 + \delta p_2 \Rightarrow \varphi_{01}\zeta - \varphi_{02}\zeta = \alpha_1 v_{01}\zeta - \alpha_2 v_{02}\zeta . \tag{A3}$$

ν_{02} can be replaced in Eq. (A3) by ν_{01} through, once again, the conservation equation (A2) leading to [using the system (A1)]

$$\frac{2(\nu_{01}-\nu_y)^{1/2}}{\kappa_1 CV^{*1/2}}(\alpha_1+\kappa'\alpha_2)\frac{s}{k} = (\alpha_1-\kappa'\alpha_2)\nu_{01} ,$$

whence comes the dispersion equation (23).

[1] J. Duran, T. Mazozi, E. Clément, and J. Rajchenbach, Phys. Rev. E **50**, 3092 (1994).

[2] J. Duran *et al.*, Phys. Rev. E **53**, 1923 (1996).

[3] F. Radjai, M. Jean, J.-J. Moreau, and S. Roux, Phys. Rev. Lett. **77**, 274 (1996).

[4] C.-H. Wang, R. Jackson, and S. Sundaresan, J. Fluid Mech. **308**, 31 (1996).

[5] M. Paczuski, S. Maslov, and P. Bak, Phys. Rev. E **53**, 414 (1996).

[6] R. Risnes, R. K. Bratli, and P. Horsrud, SPE J. **9650**, 883 (1982).

[7] M. S. Bruno, C. A. Bovberg, and R. F. Meyer, *SPE Annual Technical Conference and Exhibition, Denver, CO* (Society of Petrolum Engineers, Richardson, TX, 1996), p. 36 534.

[8] M. B. Gelikman, M. B. Dusseault, and F. A. Dullien, *SPE International Symposium for Formation Damage Control, Lafayette, LA* (Society of Petrolum Engineers, Richardson, TX, 1994), p. 27 343.

[9] E. Louis and F. Guinea, Europhys. Lett. **3**, 871 (1987).

[10] H. J. Herrmann, J. Kertesz, and L. de Arcangelis, Europhys. Lett. **10**, 147 (1989).

[11] S. Kramer and M. Marder, Phys. Rev. Lett. **68**, 205 (1992).

[12] H. Takayasu and H. Inaoka, Phys. Rev. Lett. **68**, 966 (1992); Phys. Rev. E **47**, 899 (1993).

[13] L. Prigozhin, Phys. Rev. E **49**, 1161 (1994).

[14] P. Mills, P. Cerasi, and S. Fautrat, Europhys. Lett. **29**, 215 (1995).

[15] N. Izumi and G. Parker, J. Fluid Mech. **283**, 341 (1995).

[16] P. G. Saffman and G. I. Taylor, Proc. R. Soc. London, Ser. A **245**, 312 (1958).

[17] R. A. Wooding, J. Fluid Mech. **39**, 477 (1969).

[18] R. Wittman, T. Kantzky, A. Hübler, and E. Lüscher, Naturwissenschaften **78**, 23 (1991).

[19] M. A. Carson, *The Mechanics of Erosion* (Pion, London, 1971).

[20] F. Radjai, M. Jean, J.-J. Moreau, and S. Roux, Phys. Rev. Lett. **77**, 274 (1996).

[21] J.-P. Bouchaud, M. E. Cates, and P. Claudin, J. Phys. I **5**, 639 (1995).

[22] H. A. Janssen, Z. Vereins Deutsch Ing. **39**, 1045 (1895).

[23] R. A. Bagnold, Proc. R. Soc. London, Ser. A **225**, 49 (1954).

[24] J. Rajchenbach, in *Physics of Dry Granular Matter,* edited by H. Herrmann (Kluwer, Dordrecht, 1998).

[25] J. Bear, *Dynamics of Fluids in Porous Media* (Dover, New York, 1988).

[26] This analysis was performed on a Macintosh computer using the public domain NIH IMAGE 1.55 program written by Wayne Rasband at the U. S. National Institutes of Health and available from the Internet by anonymous ftp from zippy.nimh.nih.gov or on floppy disk from NTIS, 5285 Port Royal Road, Springfield, VA 22161, part No. PB93-504868.

[27] P. Mills (unpublished).